SAND2018-3608J

Phase transition and energy storage behavior of oriented epitaxial antiferroelectric thin films

Min Gao[a], Xiao Tang[a], Chung Ming Leung[a], Steve Dai[b], Ravindranath Viswan[a], Jiefang Li[a], and D. Viehland[a]

[a] Department of Materials Science and Engineering, Virginia Tech, Blacksburg, VA 24060

[b] Sandia National Laboratories, Albuquerque, NM 87185

Abstract:

Thin films of 300-nm-thick $(Pb_{0.98}, La_{0.02})(Zr_{0.95}, Ti_{0.05})O_3$ (PLZT) were epitaxially deposited on (100), (110), and (111) $SrTiO_3$ single crystal substrates by pulsed laser deposition. X-ray diffraction line and reciprocal space mapping (RSM) scans were used to determine the crystal structure. Tetragonal ((001) PLZT) and monoclinic M_A ((011) and (111) PLZT) structures were found, which influenced the stored energy density. Electric field induced antiferroelectric to ferroelectric (AFE→FE) phase transitions were found to have a large reversible energy density of up to 30J/cm^3. With increasing temperature, an AFE to relaxor ferroelectric (AFE→RFE) transition was found. The RFE phase exhibited lower energy loss, and an improved energy storage efficiency. The results are discussed from the perspective of crystal structure, dielectric phase transitions, and energy storage characteristics.

Introduction

Many studies have focused on the electric field (E-field) induced antiferroelectric to ferroelectric (AFE→FE) phase transition. It generally exhibits unique double hysteresis loops that can increase the energy storage density and efficiency for applications in high charge energy storage devices and micro-actuators [1]. Lead zirconate titanate (PZT) is a well-investigated ABO_3 perovskite system, whose B-site cation ratio (Zr^{4+}/Ti^{4+}) can significantly alter the ferroelectric properties from AFE to FE stability [1-3]. The ratio of Zr^{4+}/Ti^{4+} = 95/5 has attracted attention as it is close to the phase boundary between AFE and FE states [2, 4, 5]. La^{3+} doping onto the Pb^{2+} site is an effective way to stabilize the AFE orthorhombic (O) phase of PZT to higher

titanium contents, over a FE rhombohedral (R) phase [2, 6]. Ten millimeter thick ($Pb_{0.88}$, $La_{0.08}$)($Zr_{0.91}$, $Ti_{0.09}$)O_3 (PLZT, 8/91/9) ceramics have been reported to have a recoverable energy storage density of 3J/cm^3, with an efficiency of 92% at an E-field of 180kV/cm [7].

To integrate with microelectronic devices, micro- and/or nano-scale PLZT films are required. Compared with bulk ceramics, thick (or thin) films have a much higher dielectric breakdown strength and saturation polarization, offering the potential for remarkable enhancements in the energy storage density [8, 9]. For example, 600-nm-thick PLZT (4/98/2) films have been reported to have a reversible energy density of 20J/cm^3 under E=1200kV/cm [8].

The induced AFE→FE phase transition in PZT ceramics exhibits a large volume change when the applied E-field exceeds a critical value of E_{FE}. Externally imposed stress/strain can thus offer an additional approach by which to modify the AFE→FE transition and transformational pathway [4, 10]. Accordingly, the lattice mismatch of PZT-based films deposited on substrates may impose significant epitaxial strains on the films, changing the AFE→FE transition process [10]. Most prior studies of epitaxial PZT (or PLZT) films have focused on compositions near the morphotropic phase boundary (MPB) between ferroelectric R and T phases (Zr^{4+}/Ti^{4+}=1) for actuator/sensor applications [11-13], or on the Ti-rich range (35/65 [14], 20/80 [15, 16], etc.) for FE memories. Little is known about the structure and properties of AFE PLZT epitaxial films. Most prior studies focused on polycrystalline AFE PZT films [4, 5, 8-10]. From the perspective of energy storage capacitor applications, polycrystalline films normally have large numbers of defects and/or grain boundaries that can reduce the dielectric breakdown strength, and thus decrease the recoverable energy density [11]. Whereas epitaxial films with lower concentrations of defects and higher mobility of domain walls can be expected to exhibit improved energy storage capability and thermostability [12].

It is known that La-doping of the PZT system weakens the FE interaction and disrupts the long-range polar order, decomposing the conventional FE domain state into

a polar nano-domain one [17, 18]. Such relaxor ferroelectrics (RFEs) have been shown to have slim and slanted P-E hysteresis loops. Low hysteresis and high saturation polarizations offer these relaxors as promising candidates for energy storage capacitor materials [19].

Here, epitaxial PLZT (2/95/5) films were deposited on different oriented $SrTiO_3$ (STO) substrates by pulsed laser deposition (PLD). The crystal structure, phase transition characteristics and pathways, and energy storage performance from room temperature to 250°C were studied, enabling a mere comprehensive understanding of PZT-based AFE films.

Experiments

Films of PLZT (2/95/5) were deposited on (100), (110), and (111) STO single-crystal substrates by PLD. A hot-pressed PLZT (2/95/5) bulk ceramic disk was used as a target material. Details of the hot-pressed process and the bulk product properties were previously reported [2]. An excimer laser LPX305i (Lambda Physik) with KrF radiation was used. The wavelength of the laser was 248nm, and the pulsed repetition rate was fixed to 5Hz. The laser energy density was fixed at 2.25J/cm^2, the oxygen partial pressure was controlled at 150mtorr, and the deposition temperature was 600°C. After deposition, the as-grown films were in-situ annealed in a pure O_2 atmosphere of 150torr at the same temperature for 30min, and then cooled to room temperature at a rate of 5°C/min. The PLZT film thickness was set at 300nm, which was confirmed by cross-sectional scanning electron microscopy (SEM, LEO 1550, Zeiss). The crystal structure was determined using a Philips X'pert high resolution X-ray diffractometer (XRD) equipped with a two bounce hybrid monochromator, and an open three-circle Eulerian cradle (resolution: 0.0002°). A pseudocubic index will be used when discussing crystal structures in this text. To obtain more structural details of the variously oriented films, reciprocal space maps (RSM) were measured along the (002), (022), and (222) zone axes. The surface topologies were determined by a Veeco SPI 3100 atomic force microscope (AFM). A homemade Sawyer-Tower system was used to measure the polarization-electric field (P-E) hysteresis loops with increasing

temperature from 25℃ to 250℃. To prevent dielectric breakdown, the maximum E-field was kept below 1000kV/cm in the low temperature range, and below 780kV/cm in the higher one. The breakdown E-field was near E=1500kV/cm at room temperature. To measure the P-E loops, a 30nm $SrRuO_3$ (SRO) buffer layer was deposited between the PLZT layer and substrate by PLD, which then served as the bottom electrode. Platinum point electrodes (40μm×40μm) were sputtered on the top surface by a Leica EM ACE600 sputter coater.

From the P-E loops, the energy storage density (ESD or U_r) was calculated by:

$$U_r = \int_{P_r}^{P_{max}} EdP; \quad (1)$$

where P_{max} and P_r are the maximum and remanent polarization, respectively [20]. The energy loss density (U_{loss}) was determined by:

$$U_{loss} = \oint PdE; \quad (2)$$

which represents the area enclosed by the P-E loops. The total energy density is the sum of U_r and U_{loss}, and the energy storage efficiency (ESE or η) was obtained by:

$$\eta = \frac{U_r}{U_r + U_{loss}} \times 100\%. \quad (3)$$

Results

(1) Structural studies

Figures 1(a)-(c) show XRD line scans along the out-of-plane (OOP) direction for PLZT films on (100), (110), and (111) STO substrates, respectively. Other XRD patterns for each sample along all three {100}, {110}, and {111} zone axes are given in Figure S1 of the supplemental materials. Well-distinguished PLZT and SRO peaks can be seen, indicating good epitaxial quality without any notable second phase signals. Figures 1(d)-(f) show 360° phi scans which were taken to determine the in-plane (IP) epitaxial relationship between the PLZT films and STO substrates. For the (001), (011), and (111) PLZT films, the epitaxial relation was (001)[100]PLZT//(001)[100]SRO//(001)[100]STO, (011)[100]PLZT//(011) [100]SRO //(011)[100]STO, and (111)[$1\bar{1}0$]PLZT//(111)[$1\bar{1}0$]SRO//(111)[$1\bar{1}0$]STO, respectively. The insets in Figures 1(a)-(c) show AFM height images, which exhibit quite smooth and dense surface morphologies with a roughness of ~2nm.

To obtain more detailed structural information, RSM mesh scans were taken after careful calibrations, as shown in Figure 2. By combining them with the XRD line scans, one can more easily determine the crystal structure and the strain condition. For (001) PLZT, doublet peaks along both the (200) and (220) zone axes were found, indicating a T structure with 90° twin domains, where the c-domain population was dominate over the a-one [21]. This domain configuration formed because it had a homogeneous IP compressive strain of -0.50% along the <100> and <010> directions, caused by a large IP lattice mismatch of -6.27% between the PLZT film (a=c=4.15A, b=4.11A for bulk PZT 95/5 [5]) and STO substrate (3.905A). Previously, Lu et. al. reported that PZT (95/5) films on (100) STO had an orthorhombic structure, similar to the bulk form, with a two-fold symmetry [5]. However, our results are notably different, as the phi scans (see Figure 1(d)) clearly evidenced a four-fold symmetry. This difference with prior results may be due to their films being thicker, and thus the epitaxial strain was capable of being fully relaxed.

For (011) and (111) PLZT films, a doublet splitting along the (200) zone axis and a triplet along the (220) zone axis were found. These are signatures of a Monoclinic type-A (M_A) crystal structure [22]. The origin of the M_A structure may be due to an inhomogeneous IP strain that tilts the c axis by a small angle: 0.37° on (110) STO, and 0.5° on (111) STO. The IP strains for the (011) PLZT were oriented along the $<01\bar{1}>$ and <100>, with values of -0.37% and -0.89%, respectively. Similar analysis was applied to the (111) PLZT film. A difference about the (222) zone was found between the (011) and (111) films, which indicated that the (111) one had a more uniform long-range polar order along the <111> direction than the other [6].

(2) P-E characteristics

Figures 3(a)-(c) show room temperature bipolar P-E loops for all three samples taken at various maximum E-fields. The asymmetry of the electrodes (bottom: SRO; top: Pt) resulted in loop drifting, as reported in several prior PZT film studies [23, 24]. Figures 3(d)-(f) give the calculated ESD and ESE values as a function of E. Under low E-fields ($E \leq 280$kV/cm), all three samples exhibited typical AFE loops with a small

remanent polarization, low P-E loop areas (i.e. low loss), and hence a relatively high ESE. As the maximum E was increased, a critical field E_{FE} was reached, where the AFE→FE phase transition was induced. For (001), (011), and (111) PLZT films, the values of E_{FE} were about 330kV/cm, 320kV/cm, and 285kV/cm, respectively. Please note that measurements were carried out only along the OOP direction, which is the [001] for (001) PLZT, [011] for (011), and [111] for (111). In bulk PZT samples, the sub-lattice interaction of the AFE phase is along the <110> direction. The easy axis of the spontaneous polarization is along [001] direction for T structure, and along the (110) plane for M_A (see Figure 1(g)). In bulk materials, the AFE→FE transition results in a O→R phase transition, where the easy polarization axis of R is along $(111)_{pc}$. These observations, along with the strain effects, may explain the differences in the EFE values [8, 25].

The remanent polarizations of the (001), (011), and (111) PLZT films were about 16μC/cm^2, 34μC/cm^2, and 17μC/cm^2, respectively. These values are notably larger than that of bulk AFE PLZT samples, indicating a higher tendency to retain FE order at zero E-field after the AFE→FE transition has been induced [9, 26]. This may be due to the film/electrode interface layer, and/or residual stress/strain condition [27-29]. The saturation polarizations of all three films were exceptionally high, having values of about 70μC/cm^2, which will enable higher ESD values. From the shape of the P-E loops, it can be seen that (111) PLZT had the steepest slope at the inflection point, relative to either (001) or (011). Correspondingly, Figures 3(d)-(f) show that (111) PLZT had the highest ESD (~40J/cm^3) and ESE (~53%) values, compared to (001) PLZT (~27J/cm^3, ~40%) and (011) PLZT (~16J/cm^3, ~22%). Figures S2 (a)-(c) show the frequency (f) dependent P-E loops taken at room temperature. The curves were stable for 10kHz≤f≤100kHz in all three oriented films, which shows their capabilities of the working frequency range of typical pulsed capacitor devices [7]. The changes in the P-E loops at lower frequencies are probably caused by leakage currents with decreasing AC frequencies [30]. Since our samples were more stable at higher frequencies, the below measurements were all obtained at 100kHz.

(3) Dependence of structure and FE properties on temperature

Next, the P-E loops were measured at various temperatures on heating from 25℃ to 250℃. They reveal an AFE/FE→RFE transition in each case. A panel of chosen P-E loops is shown in Figure 4. These data demonstrate that the waisted P-E loops with significant hysteretic area became slim loops with increasing temperature. The slim loops are indicative of RFE characteristics. Details of these changes in P-E loops were different for (001) PLZT relative to the other two, but the generalities were the same. For (001) PLZT, a waisted AFE/FE P-E loop became a slim (RFE) one on heating from 70℃ to 100℃. Whereas, for (011) and (111) PLZT films, the waisted AFE/FE loops first transited to typical FE loops on heating (50~70℃ for (011) PLZT, and 100~125℃ for (111) PLZT), and then gradually evolved into slim (RFE) type ones with further increase of temperature. Once in the slim loop (RFE phase) state, their coercivity (E_C) was continuously reduced with increasing temperature to 250℃, as can be seen in Figure 5. This gradual decrease in E_C is typical of a diffuse transformation from FE to paraelectric (PE) phases [6, 31]. Figure 4 also evidences that the PLZT films remained in the RFE phase until a temperature above 250℃, demonstrating that the Curie temperature range was increased to higher temperatures compared to the bulk (about 230℃ [2]). This can be attributed to epitaxial strain effects, which may stabilize the polar phase to higher temperatures and thus extend the working range of the RFE phase of the PLZT films [30, 32].

Values for the ESD, ESE, and remanent polarization were calculated from the P-E loops. The results are summarized as functions of both temperature and E in Figure 6. The saturation polarization, energy loss, and total energy density are given in Figure S3 of the supplemental materials. Similar phase transition trends were found for the three samples. For E≤600kV/cm, all three samples exhibited relatively stable values of ESD over the temperature range between 25℃ and 250℃. Small changes are probably due to increased leakage currents caused by higher oxygen vacancy mobility at higher temperatures. However, under higher E, the three samples exhibited different changes in ESD, which can be explained by differences in their phase transformational pathways,

as discussed above. For (001) PLZT, as the temperature was increased, the ESD value was slightly decreased in the AFE/FE region. It increased from 20J/cm^3 to 35J/cm^3 above the AFE/FE→RFE transition, and then remained relatively high with further increase of temperature in the RFE region. For (011) PLZT, the value of ESD decreased with increasing temperature in the AFE/FE→FE transformational region from 18J/cm^3 to 15J/cm^3, and then increased back to 18J/cm^3 upon heating into the FE→RFE transition range. The (111) PLZT film exhibited similar relative trends with increasing temperature as for the (011) film, although its values of ESD were higher. Initially, the ESD decreased dramatically from 40J/cm^3 to 17J/cm^3 upon heating into the AFE/FE→FE transitional region. This value remained low on heating until 180°C within the FE region, and then increased to 25J/cm^3 on further heating to 250°C in the RFE region.

The value of ESE (see Figures 6 (d)-(f)) exhibited opposite trends to that of the remanent polarization (see Figures 6 (g)-(i)). This indicates that the efficiency is affected not only by ESD, but also by the energy losses during a charge/discharge cycle, which is strongly related to the samples' remanent polarization. Accordingly, in the FE region, the (011) and (111) PLZT films had notably lower efficiencies; whereas, in the other phase regions, the efficiencies of these three samples remained high. The drop in efficiency at higher temperatures and higher E-fields is probably due to increased leakage currents. Figure 6 summarizes the proper working temperature ranges for the differently oriented PLZT films, where each film offers its highest ESD and ESE values: 70~200°C for (001) PLZT (25~35J/cm^3, 50~70%), 150~200°C for (011) PLZT (12~18J/cm^3, 30~50%), and both 25°C to 70°C and 200~250°C for (111) PLZT (20~40J/cm^3, 30~55%).

Temperature variable XRD data were then taken to determine the crystal structure and lattice parameter changes. XRD line scans (see Figures 7 (a)-(b)) show that the left side of the PLZT peaks did not change much with increasing temperature. Rather, the right side of the peaks continuously shifted to smaller 2theta values with increasing temperature, and finally merged with the left peaks near 250°C. The RSM scans

demonstrated that the crystal structure did not change for any of these films over the temperature range investigated (see Figures 7 (c)-(f)). The temperature dependence of the lattice parameters for both PLZT and STO are shown in Figures 7 (g)-(i). The lattice parameter of STO was linearly extended with increasing temperature due to thermal expansion. This may partially relax the lattice mismatch between itself and the films, reducing the IP strain of the PLZT layers. No evidence of sudden changes in the c/a ratio of the PLZT films was observed until above 200°C. On the contrary, the value of c/a gradually approached one as the temperature was increased towards 250°C. Temperature variable XRD results indicate that the changes in P-E characteristics with temperature discussed above can be attributed to the reduction of the tetragonality or monoclinicity, which are more likely strain-induced transitions rather than symmetry-related ones [33].

(4) Unipolar drive and energy storage characteristics

The PLZT films contained a mixed AFE/FE phase stability, after bipolar drive, as evidence by the large values of P_r for E=0. Thus, on reversal of applied E-field polarity, the polarization rotation in the FE regions may consume more energy. This, in turn, diminishes the ESE. In domain-engineered piezoelectric crystals, unipolar drive has been shown as an effective way to decrease hysteretic losses and energy consumption [34, 35]. Furthermore, under unipolar drive, since the polarity of E does not switch, defects such as oxygen vacancies will not continuously migrate, favoring to improve fatigue limits for high-frequency charging/discharging cycles, and accordingly reducing the leakage current's reduction of the ESE value.

As shown in Figures 8 (a)-(c), under unipolar drive, the remanent polarization was noticeably smaller than those under bipolar drive. At the same time, the ESD values (see Figures 8 (d)-(f)) were considerably more stable than the bipolar ones over the entire temperature range studied. The maximum ESD values were about 19J/cm^3, 15J/cm^3, and 17J/cm^3 for (001) PLZT, (011) PLZT, and (111) PLZT, respectively. These are comparable to the bipolar results, when considering the fact that the unipolar cycle was half of the bipolar one. Due to the lower remanent polarization values in the

unipolar cases, the ESE values in Figures 8 (g)-(i) were significantly higher than the bipolar ones, in particular for the (011) film. The efficiency at the maximum ESD value reached 77%, 60%, and 70% for (001), (011), and (111) PLZT, respectively. All three samples exhibited a gradual AFE/FE-RFE transformation with increasing temperature.

With respect to applications, fatigue limit tests of these PLZT films revealed that the energy storage performance characteristics could be maintained after 10^8 charging/discharging cycles under a maximum field of 765kV/cm and at room temperature, as shown in Figure 9. This is different from induced AFE→FE transitions in bulk, where large c/a ratio changes result in rapid deterioration of the samples' mechanical intensities with cycles. Clearly, unipolar drive may be a promising way to enhance the energy storage capability of AFE thin film materials for pulsed capacitors.

Discussion and summary

Intermediate T phases have previously been reported in $PbZrO_3$ ceramics and crystals [2, 36], which have been found only over narrow temperature ranges (about 5°C) sandwiched between the cubic (C) and AFE orthorhombic (AFE_O) ones. It has remained controversial whether this T phase is stable or metastable, and whether it has FE or AFE order [2, 10, 37, 38]. Previous studies by Dai et al. revealed ferroelectric P-E hysteresis loops in this intermediate phase field [2]. Here, our findings for (001) PLZT (2/95/5) demonstrate that both AFE_T and FE_T phases can be stabilized by epitaxial strain. The phase transformational sequence on heating is then $AFE_T \rightarrow RFE_T \rightarrow C$. Furthermore, a new monoclinic M_A phase region has been found in high Zr-content PLZT, which was previously unknown. Our data demonstrate that (011) and (111) PLZT (2/95/5) has both AFE_{MA} and FE_{MA} phases that are stabilized by epitaxial strain. The phase transformational sequence on heating is then $AFE_{MA} \rightarrow FE_{MA} \rightarrow RFE_{MA} \rightarrow C$. Clearly, the phase stability on the AFE side of the PLZT (and PZT) systems can be significantly altered by epitaxial engineering.

The fact that the crystal structure remains either T or M_A during the AFE→FE transition results in the transformational strains being negligible compared to that for bulk samples. Correspondingly, the energy storage efficiency does not degrade with

repeated cycling of the field for $\geq 10^8$ times, and the film remains mechanically robust.

Heating in all cases resulted in an AFE→FE transition. Further increase in temperature within the FE phase region resulted in slim hysteresis loops, typical of relaxor ferroelectrics. Slim P-E hysteresis loops have previously been reported at elevated temperatures in Sn-doped PZT (PZST) [25, 39], and PLZT ceramics that undergo an $AFE_O \rightarrow FE_R \rightarrow C$ transformational sequence. Substitution by La was shown a breakup of the long range translation symmetry of the polarization in the FE_R state of this sequence, favoring the RFE and polar nanodomain state [17, 18, 40]. Our findings here are consistent with this perspective. The principle difference between the various orientations of epitaxial PLZT (2/95/5) thin layers is the temperature at which the slim loop RFE phase appears on heating in the transformational sequence.

Comparisons of the bipolar and unipolar P-E loops at room temperature will reveal an important consideration for all oriented PLZT films studied. The value of P_r (after cycling through saturation) was notably higher under bipolar drive (15-30μC/cm^2) compared to unipolar (~5μC/cm^2). The same value of saturation ($P_s \approx 70\mu C/cm^2$) was achieved in both cases. As a consequence, the double loop characteristics were not as evident under bipolar drive, as for the unipolar. We believe that this is due to the close proximity of the RFE state characterized by polar nanoregions (PNRs). In fact, in high Zr-content PLZT ceramics, PNRs have previously been found to coexist with AFE_O domain modulations whose wave vectors were nearly the same size as the PNRs [41, 42]. Investigations of poled piezoelectric single crystals of $Pb(Mg_{1/3}Nb_{2/3})O_3$-xat%$PbTiO_3$ have previously shown that the rearrangement of PNRs within the geometrical restrictions imposed by the elastic compatibility conditions results in reduced hysteresis under unipolar drive, whereas reversing the direction of polarization under bipolar drive results in large hysteresis losses [34, 43]. Here, in this investigation, since the AFE and FE phases have the same crystal structure, the AFE modulations and PNRs could easily arrange into geometrical patterns that achieve compatibility under unipolar drive, reducing hysteretic losses compared to the bipolar case where renucleation of PNRs under reversed drive would occur.

This has important implications for explaining the differences in the ESD and ESE of the various oriented PLZT (2/95/5) thin films under bipolar and unipolar drive. Under bipolar drive, the films have ESD values that varied with temperature and orientation. This reflects changes not only due to phase transitions, but also changes in P_r. However, under unipolar drive, the films had quite stable values of ESD as a function of temperature between 25 and 250°C at set field levels. Correspondingly, the ESEs were higher and more stable under unipolar drive within individual AFE, FE, and RFE phase regions.

In summary, thin films of PLZT (2/95/5) were epitaxially deposited on (100), (110), and (111) STO substrates. An orientation effect imparted to the PLZT films, via diverse values of the IP strains, resulted in either T phase stability for PLZT on (100) STO or M_A phase for PLZT on (110) and (111) STO. The interrelationship amongst crystal structure, dielectric phase transitions, and energy storage performance was studied over the temperature range from 25 to 250°C. The (001) PLZT films exhibited an $AFE_T/FE_T \rightarrow RFE_T$ transition under E, where the bipolar drive resulted in an ESD of $\geq 35 J/cm^3$ and an ESE of ≥70%. The (011) and (111) PLZT films exhibited an $AFE_{MA}/FE_{MA} \rightarrow FE_{MA} \rightarrow RFE_{MA}$ transition, but their ESD (ESE) values only reached $\leq 18 J/cm^3$ (50%) and $\leq 40 J/cm^3$ (55%), respectively. Investigations under unipolar drive were also performed, revealing notably higher ESE values due to low energy losses.

Reference

1. Uchino K, Nomura S. Electrostriction in PZT-family antiferroelectrics[J]. Ferroelectrics, 1983, 50(1): 191-196.

2. Dai X. New perspectives of pure and lanthanum modified lead zirconate titanate crystalline solutions[D]. University of Illinois at Urbana-Champaign, 1995.

3. Noheda B, Cox D E, Shirane G, et al. A monoclinic ferroelectric phase in the Pb (Zr 1− x Ti x) O 3 solid solution[J]. Applied physics letters, 1999, 74(14): 2059-2061.

4. Zuo Z H, Zhan Q F, Chen B, et al. Enhanced energy storage behaviors in free-standing antiferroelectric Pb (Zr0. 95Ti0. 05) O3 thin membranes[J]. Chinese Physics B, 2016, 25(8): 087702.

5. Lu C J, Shen H M, Wang Y N. The growth and phase transitions of epitaxial Pb (Zr0. 95Ti0. 05) O3 thin films prepared by sputter deposition combined with post-annealing on SrTiO3 (1 0 0)[J]. Journal of crystal growth, 1998, 191(1-2): 113-118.

6. Gupta S M, Li J F, Viehland D. Coexistence of Relaxor and Normal Ferroelectric Phases in Morphotropic Phase Boundary Compositions of Lanthanum-Modified Lead Zirconate Titanate[J]. Journal of the American Ceramic Society, 1998, 81(3): 557-564.

7. Jo H R, Lynch C S. A high energy density relaxor antiferroelectric pulsed capacitor dielectric[J]. Journal of Applied Physics, 2016, 119(2): 024104.

8. Pan H, Zeng Y, Shen Y, et al. Thickness-dependent dielectric and energy storage properties of (Pb0. 96La0. 04)(Zr0. 98Ti0. 02) O3 antiferroelectric thin films[J]. Journal of Applied Physics, 2016, 119(12): 124106.

9. Ma B, Kwon D K, Narayanan M, et al. Dielectric properties and energy storage capability of antiferroelectric Pb 0.92 La 0.08 Zr 0.95 Ti 0.05 O 3 film-on-foil capacitors[J]. Journal of Materials Research, 2009, 24(9): 2993-2996.

10. Ge J, Remiens D, Dong X, et al. Enhancement of energy storage in epitaxial PbZrO3 antiferroelectric films using strain engineering[J]. Applied Physics Letters, 2014, 105(11): 112908.

11. Hu G, Ma C, Wei W, et al. Enhanced energy density with a wide thermal stability in epitaxial Pb0. 92La0. 08Zr0. 52Ti0. 48O3 thin films[J]. Applied Physics Letters, 2016, 109(19): 193904.

12. Ma C, Ma B, Mi S B, et al. Enhanced dielectric nonlinearity in epitaxial Pb0. 92La0. 08Zr0. 52Ti0. 48O3 thin films[J]. Applied Physics Letters, 2014, 104(16): 162902.

13. Vu H T, Nguyen M D, Houwman E, et al. Ferroelectric and piezoelectric responses of (110) and (001)-oriented epitaxial Pb (Zr0. 52Ti0. 48) O3 thin films on all-oxide layers buffered silicon[J]. Materials research bulletin, 2015, 72: 160-167.

14. Saito K, Kurosawa T, Akai T, et al. Structural characterization and 90 domain contribution to ferroelectricity of epitaxial Pb (Zr 0.35, Ti 0.65) O 3 thin films[J]. Journal of Applied Physics, 2003, 93(1): 545-550.

15. Lee H N, Nakhmanson S M, Chisholm M F, et al. Suppressed dependence of polarization on epitaxial strain in highly polar ferroelectrics[J]. Physical review letters, 2007, 98(21): 217602.

16. Chisholm M F, Luo W, Oxley M P, et al. Atomic-scale compensation phenomena at polar interfaces[J]. Physical review letters, 2010, 105(19): 197602.

17. Thomas N W. A new framework for understanding relaxor ferroelectrics[J]. Journal of Physics and Chemistry of Solids, 1990, 51(12): 1419-1431.

18. Li J F, Dai X, Chow A, et al. Polarization switching mechanisms and electromechanical properties of La-modified lead zirconate titanate ceramics[J]. Journal of materials research, 1995, 10(4): 926-938.

19. Li B, Liu Q X, Tang X G, et al. Antiferroelectric to relaxor ferroelectric phase transition in PbO modified (Pb 0.97 La 0.02)(Zr 0.95 Ti 0.05) O 3 ceramics with a large energy-density for dielectric energy storage[J]. RSC Advances, 2017, 7(68): 43327-43333.

20. Burn I, Smyth D M. Energy storage in ceramic dielectrics[J]. Journal of Materials Science, 1972, 7(3): 339-343.

21. Kim Y K, Morioka H, Funakubo H. Domain structures in highly (100)-

oriented epitaxial Pb (Zr 0.35, Ti 0.65) O 3 thin films[J]. Journal of applied physics, 2007, 101(6): 064112.

22. Chen Z, Luo Z, Huang C, et al. Low-Symmetry Monoclinic Phases and Polarization Rotation Path Mediated by Epitaxial Strain in Multiferroic BiFeO3 Thin Films[J]. Advanced Functional Materials, 2011, 21(1): 133-138.

23. Baek S H, Park J, Kim D M, et al. Giant piezoelectricity on Si for hyperactive MEMS[J]. Science, 2011, 334(6058): 958-961.

24. Warusawithana M P, Cen C, Sleasman C R, et al. A ferroelectric oxide made directly on silicon[J]. Science, 2009, 324(5925): 367-370.

25. Sharifzadeh Mirshekarloo M, Yao K, Sritharan T. Large strain and high energy storage density in orthorhombic perovskite (Pb 0.97 La 0.02)(Zr 1− x− y Sn x Ti y) O 3 antiferroelectric thin films[J]. Applied Physics Letters, 2010, 97(14): 142902.

26. Kong L B, Ma J. Preparation and characterization of antiferroelectric PLZT2/95/5 thin films via a sol–gel process[J]. Materials Letters, 2002, 56(1-2): 30-37.

27. Xu B, Ye Y, Wang Q M, et al. Dependence of electrical properties on film thickness in lanthanum-doped lead zirconate titanate stannate antiferroelectric thin films[J]. Journal of applied physics, 1999, 85(7): 3753-3758.

28. Larsen P K, Dormans G J M, Taylor D J, et al. Ferroelectric properties and fatigue of PbZr0. 51Ti0. 49O3 thin films of varying thickness: Blocking layer model[J]. Journal of applied physics, 1994, 76(4): 2405-2413.

29. Chen H D, Li K K, Gaskey C J, et al. Thickness-dependent electrical properties in lanthanum-doped PZT thick films[J]. MRS Online Proceedings Library Archive, 1996, 433.

30. Bharadwaja S S N, Krupanidhi S B. Dielectric relaxation in antiferroelectric multigrain PbZrO3 thin films[J]. Materials Science and Engineering: B, 2000, 78(2-3): 75-83.

31. Hao X, Wang Y, Yang J, et al. High energy-storage performance in Pb0. 91La0. 09 (Ti0. 65Zr0. 35) O3 relaxor ferroelectric thin films[J]. Journal of applied physics, 2012, 112(11): 114111.

32. Pertsev N A, Zembilgotov A G, Tagantsev A K. Effect of mechanical boundary conditions on phase diagrams of epitaxial ferroelectric thin films[J]. Physical review letters, 1998, 80(9): 1988

33. Kang S J, Joung Y H. Fatigue, retention and switching properties of PLZT (x/30/70) thin films with various La concentrations[J]. Journal of materials science, 2007, 42(18): 7899-7905.

34. Viehland D. Effect of uniaxial stress upon the electromechanical properties of various piezoelectric ceramics and single crystals[J]. Journal of the American Ceramic Society, 2006, 89(3): 775-785.

35. Viehland D, Powers J. Effect of uniaxial stress on the electromechanical properties of 0.7 Pb (Mg 1/3 Nb 2/3) O 3–0.3 PbTiO 3 crystals and ceramics[J]. Journal of Applied Physics, 2001, 89(3): 1820-1825.

36. Jaffe, B., W. J. Cook, and H. Jaffe, Piezoelectric Ceramics. Academic Press, London (1971).

37. Scott B A, Burns G. Crystal growth and observation of the ferroelectric phase of PbZrO3[J]. Journal of the American Ceramic Society, 1972, 55(7): 331-333.

38. Zhai J, Yao Y, Li X, et al. Dielectric properties of oriented PbZrO 3 thin films grown by sol-gel process[J]. Journal of applied physics, 2002, 92(7): 3990-3994.

39. Hao X, Zhai J, Yao X. Improved Energy Storage Performance and Fatigue Endurance of Sr - Doped PbZrO3 Antiferroelectric Thin Films[J]. Journal of the American Ceramic Society, 2009, 92(5): 1133-1135.

40. Dai X, Viehland D. Effects of lanthanum modification on the antiferroelectric - ferroelectric stability of high zirconium - content lead zirconate titanate[J]. Journal of applied physics, 1994, 76(6): 3701-3709.

41. Bokov A A, Ye Z G. Recent progress in relaxor ferroelectrics with perovskite structure[M]//Frontiers of Ferroelectricity. Springer US, 2006: 31-52.

42. Viehland D, Dai X H, Li J F, et al. Effects of quenched disorder on La-modified lead zirconate titanate: long-and short-range ordered structurally incommensurate phases, and glassy polar clusters[J]. Journal of applied physics, 1998,

84(1): 458-471.

43. Dkhil B, Gemeiner P, Al-Barakaty A, et al. Intermediate temperature scale T∗ in lead-based relaxor systems[J]. Physical Review B, 2009, 80(6): 064103.

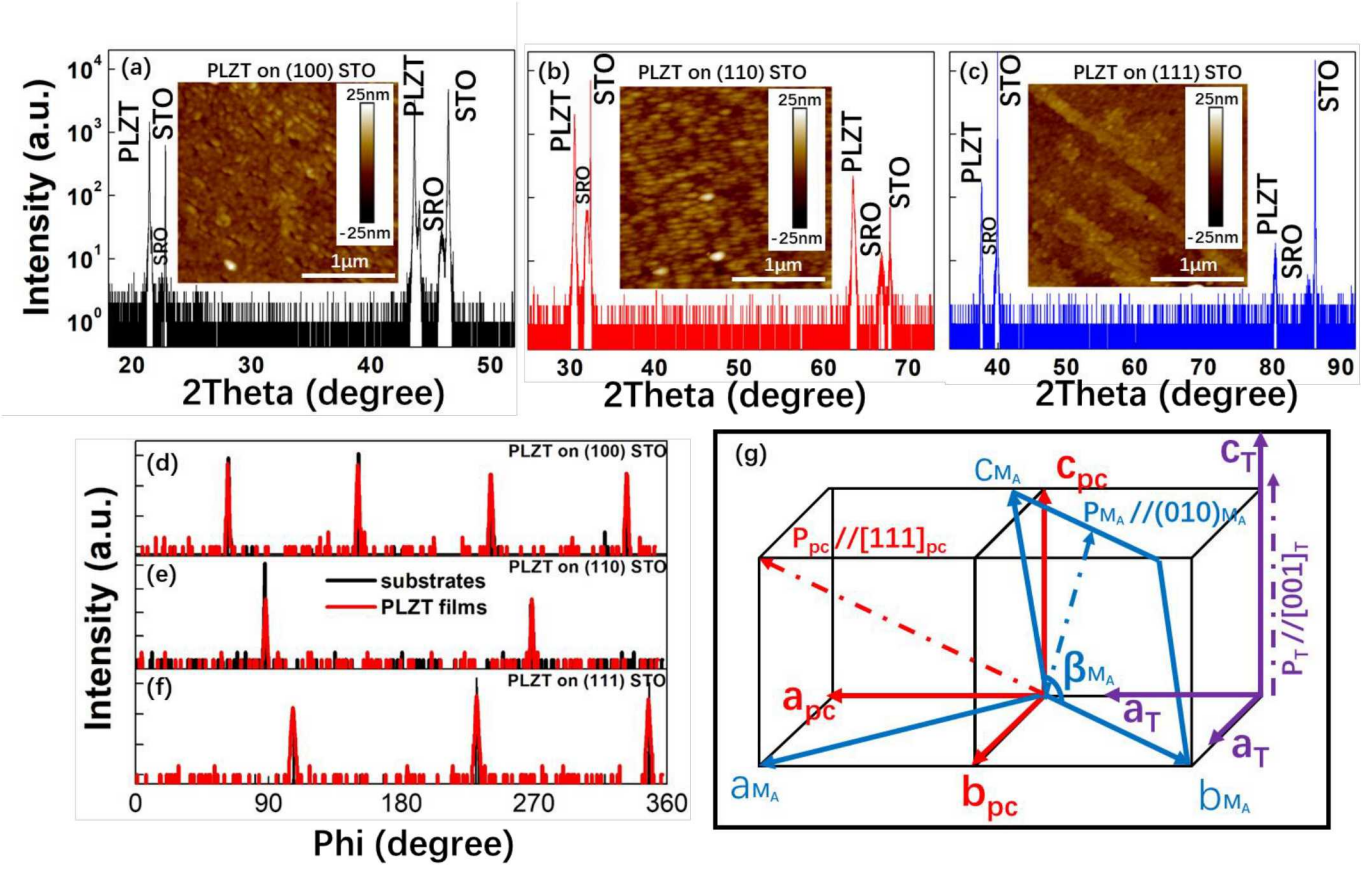

Figure 1. XRD line scans patterns of 300nm PLZT films on (a), (d) (100) STO; (b), (e) (110) STO; and (c), (f) (111) STO substrates. Parts (a)-(c) show 2theta scans, and Parts (d)-(f) show phi scans. The insets in (a)-(c) are the corresponding AFM height images of the PLZT films. Part (g) shows a schematic illustration of the monoclinic and tetragonal crystal structures, along with their polarization directions.

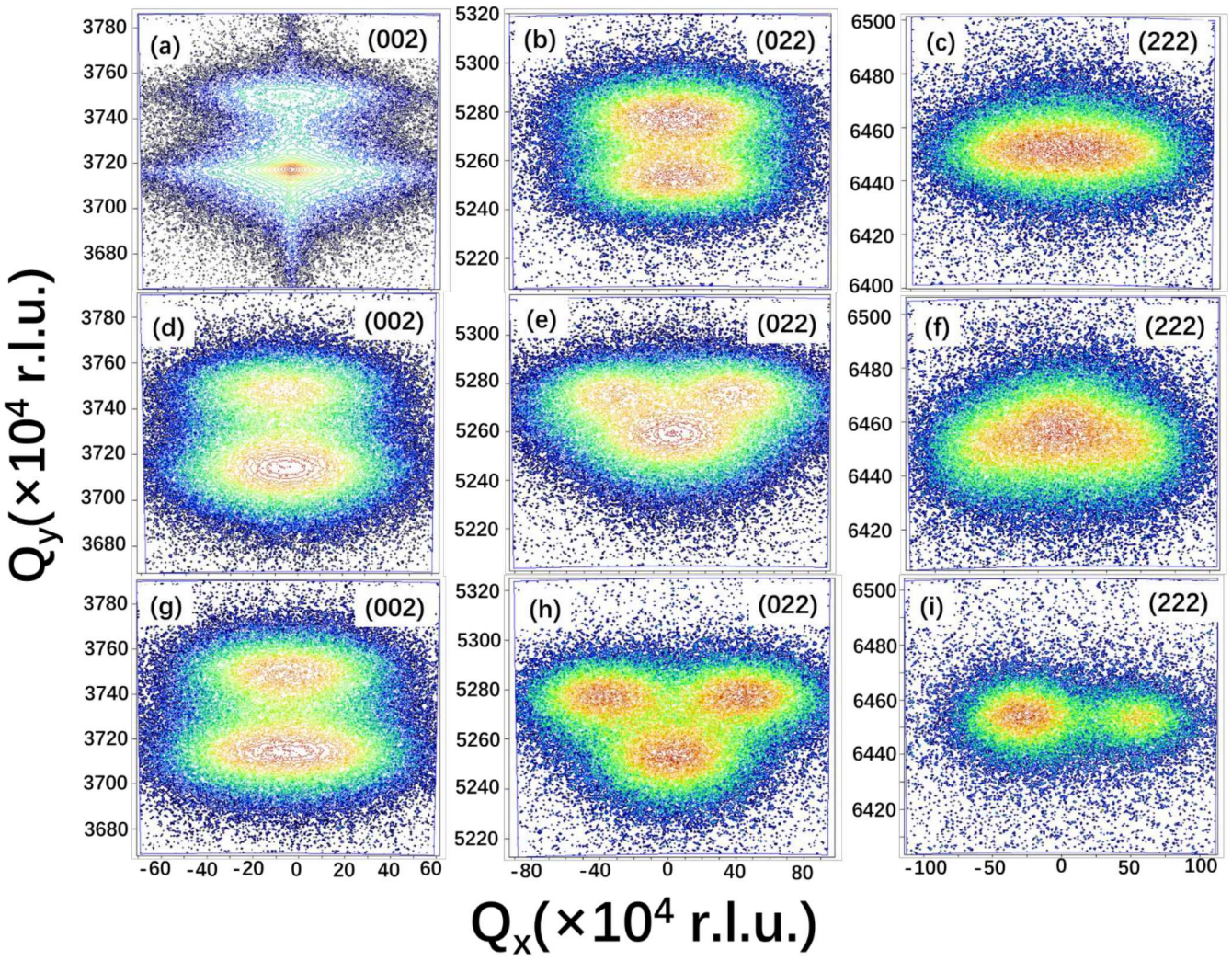

Figure 2. RSM images of (a)-(c) (001) PLZT film, (d)-(f) (011) PLZT film, and (g)-(i) (111) PLZT film. (a), (d), (g) were taken along the (002) zone axis; (b), (e), (h) along the (022) zone axis; and (c), (f), (i) along the (222) zone axis.

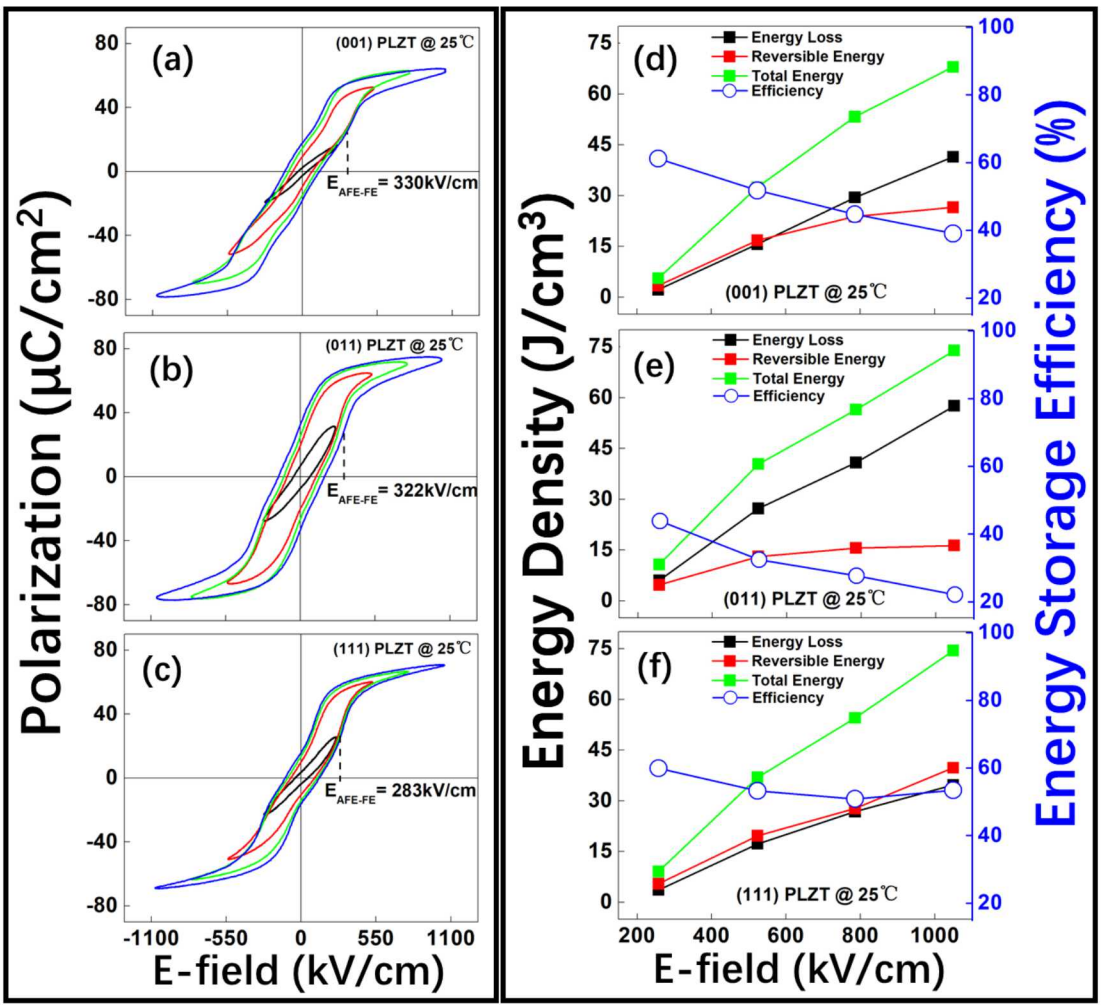

Figure 3. P-E loops of (a) (001) PLZT, (b) (011) PLZT, and (c) (111) PLZT at room temperature with increasing E-fields. Parts (d)-(f) show the corresponding energy densities and ESE values calculated from (a)-(c).

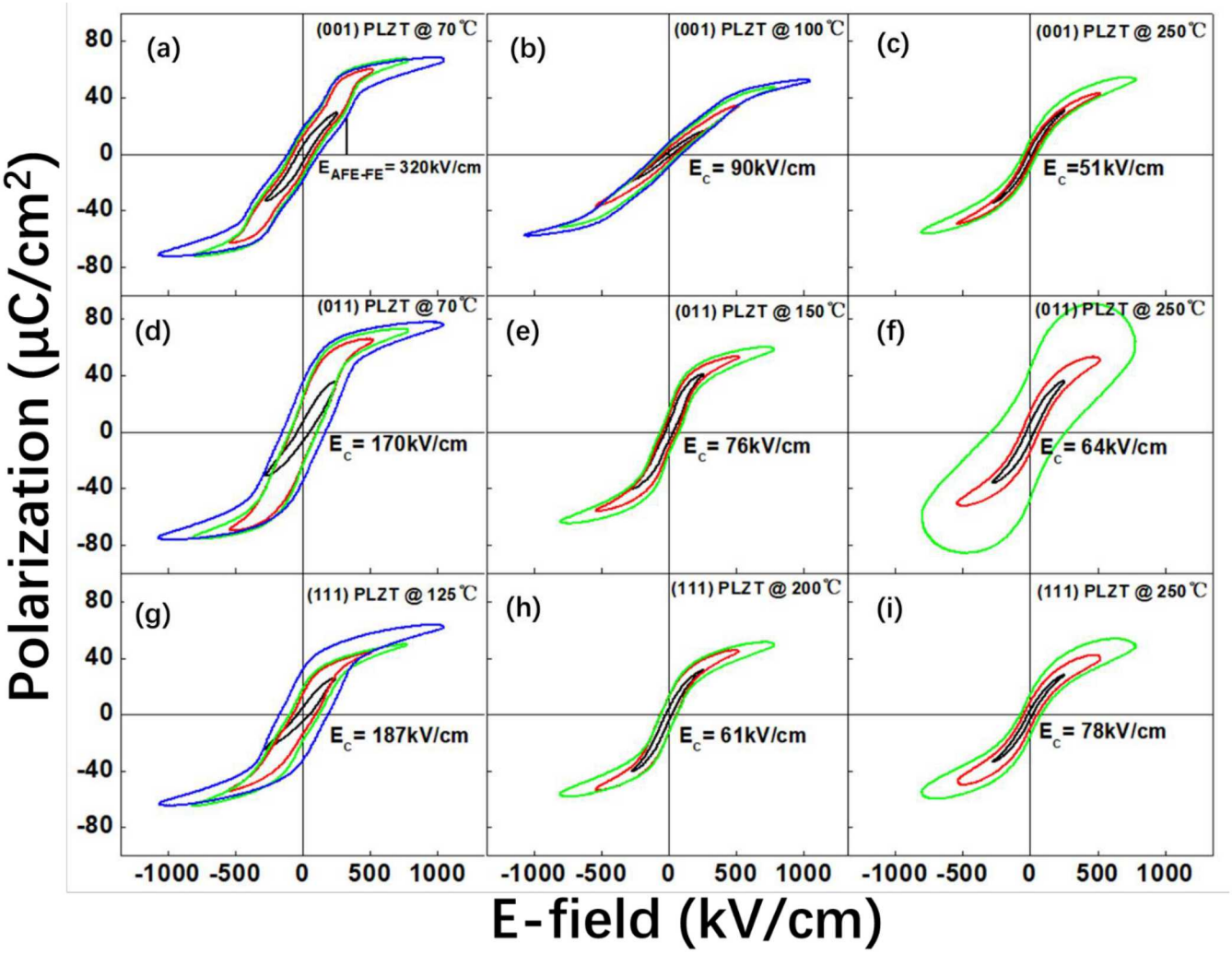

Figure 4. P-E loops of (a)-(c) (001) PLZT, (d)-(f) (011) PLZT, and (g)-(i) (111) PLZT measured at various temperatures that reveal different ferroelectric phase stabilities: (a) AFE; (d), (g) FE, and others are RFE. The wider loops in (f) and (i) were caused by leakage currents.

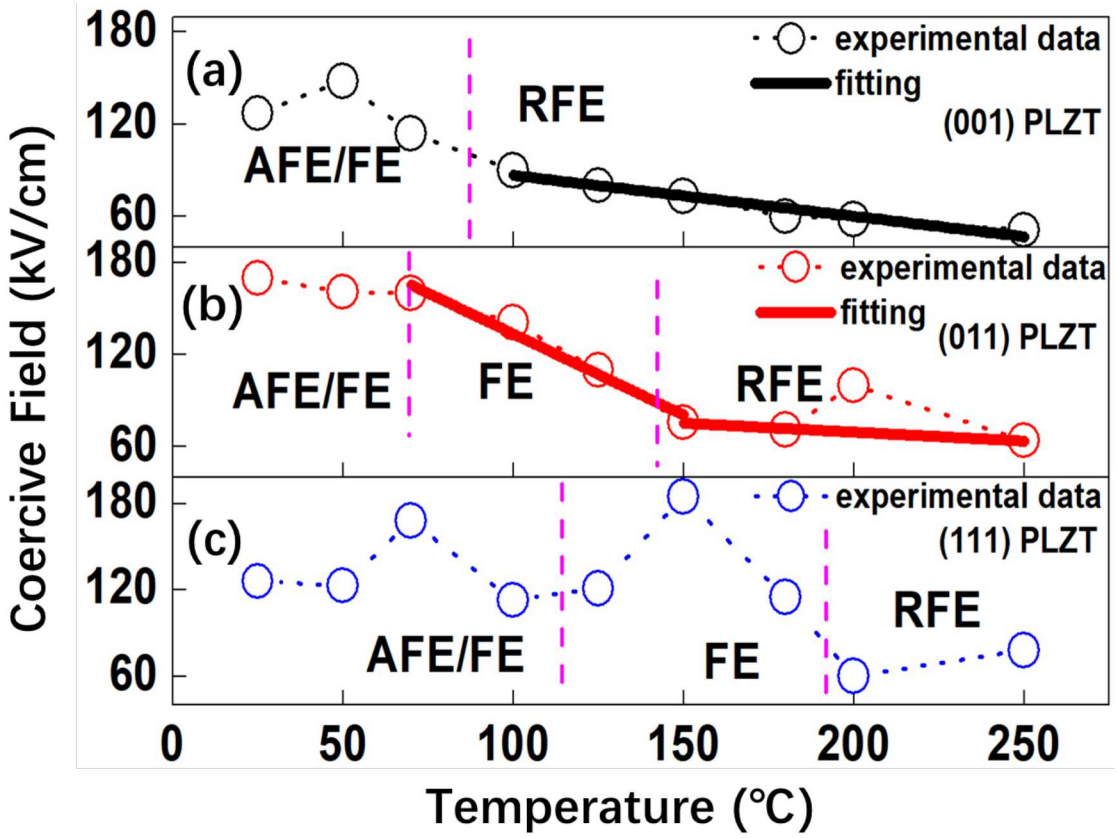

Figure 5. Coercive field of (a) (001) PLZT, (b) (011) PLZT, and (c) (111) PLZT as function of the temperature. Dotted lines are experimental data, and solid ones are the fitting results. The purple dash lines separate different phase regions based on their P-E loop characteristics.

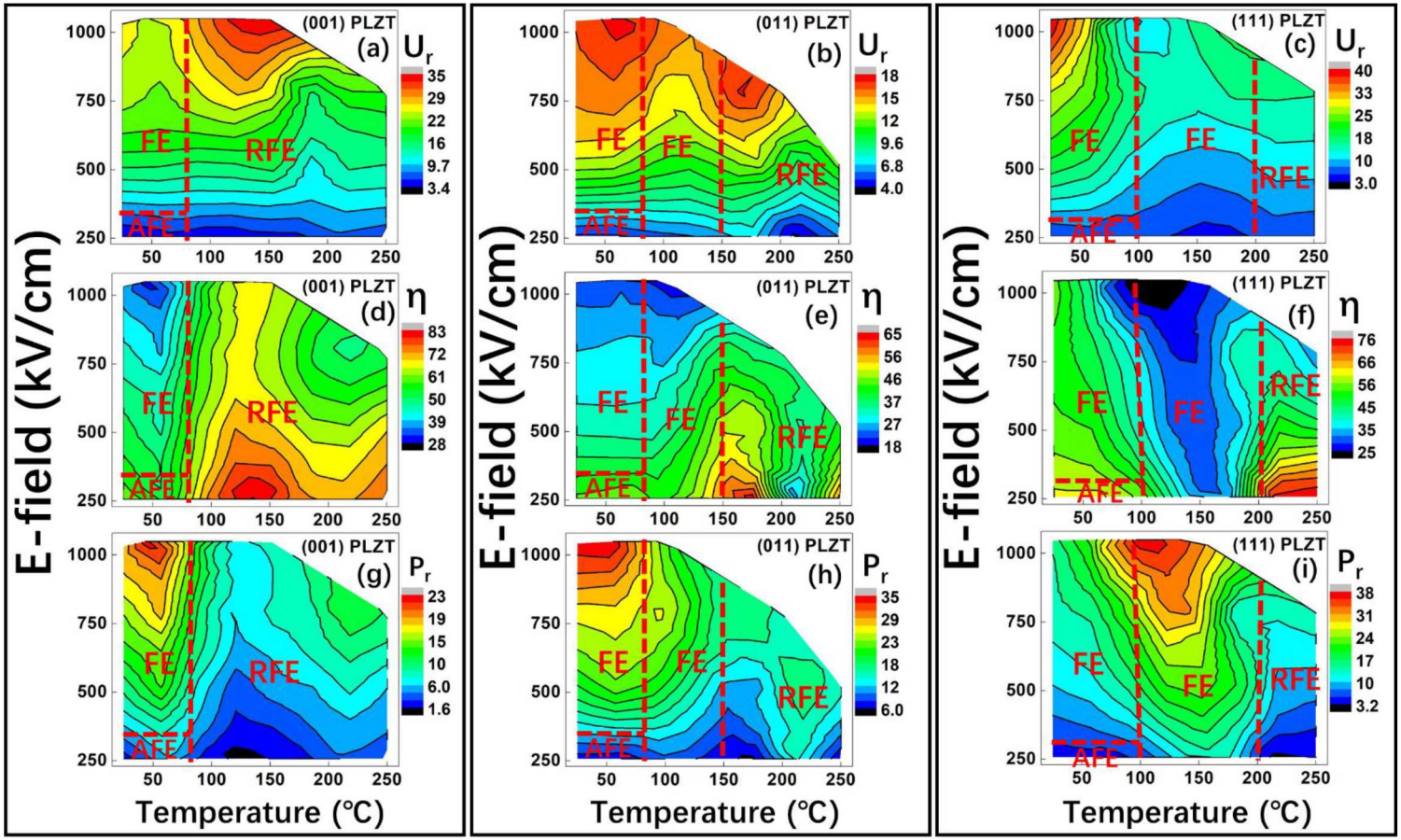

Figure 6. (a)-(c) ESD (J/cm^3), (d)-(f) ESE (%), and (g)-(i) remanent polarization (μC/cm^2) of oriented PLZT films as functions of both E and temperature. (a), (d), (g) (001) PLZT; (b), (e), (h) (011) PLZT; and (c), (f), (i) (111) PLZT. Different phase regions are marked by red dash lines in each figure.

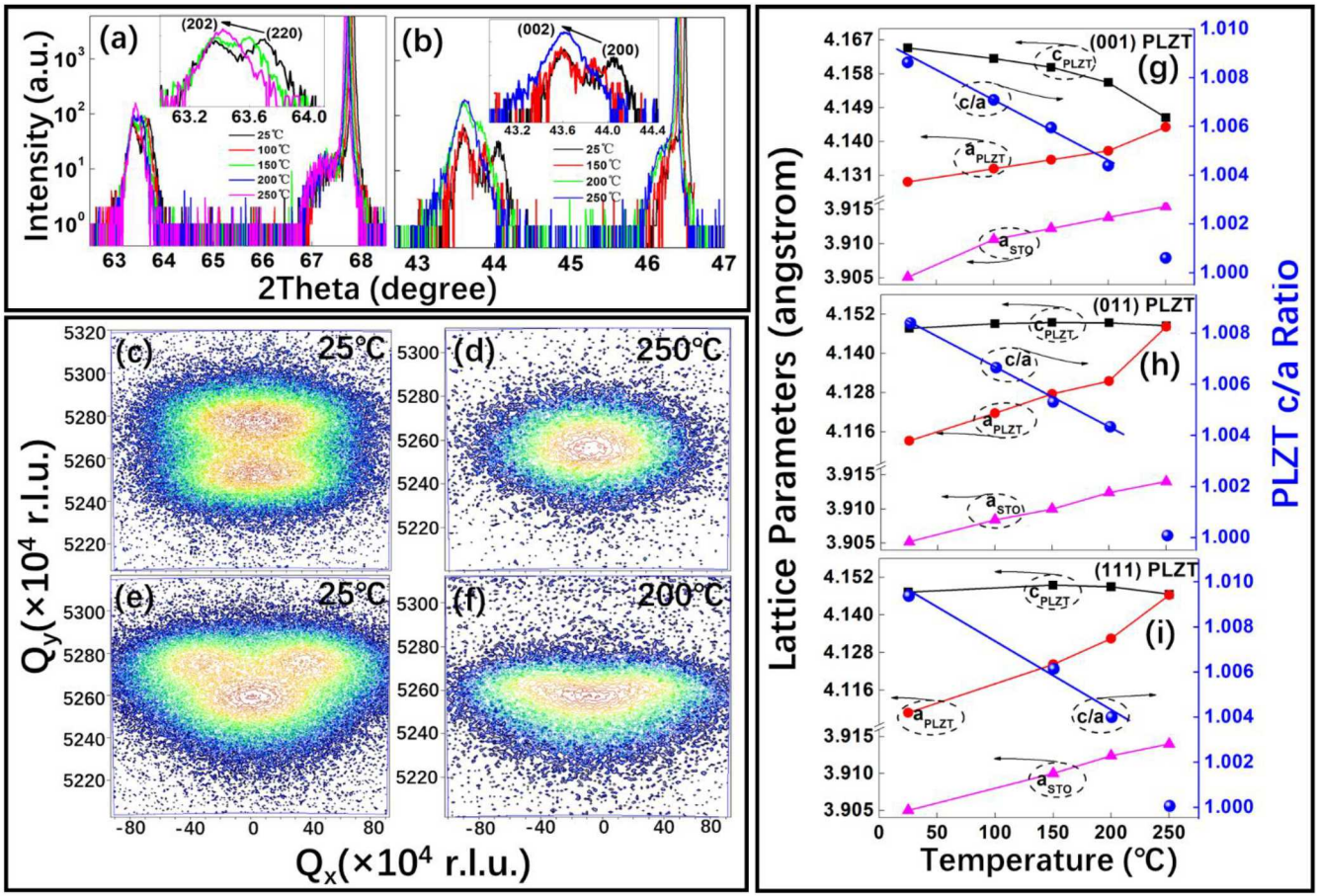

Figure 7. Temperature dependent XRD line scans of (a) PLZT/SRO on (001) STO, and (b) PLZT/SRO on (111) STO. Parts (c)-(f) RSM images of (c), (d) (001) PLZT; and (e), (f) (011) PLZT. The zone axis is along the (022) in (a), (c)-(f); and along the (002) in (b). (g)-(i) Calculated lattice parameters of STO substrate (a_{STO}) and PLZT film (a_{PLZT}, c_{PLZT}), as well as the c/a ratio of PLZT, as a function of temperature. The orientations of the substrate in (g), (h), and (i) are (100), (110), and (111), respectively. The c/a ration of PLZT was linearly fitted to temperature in the range from 25°C to 200°C.

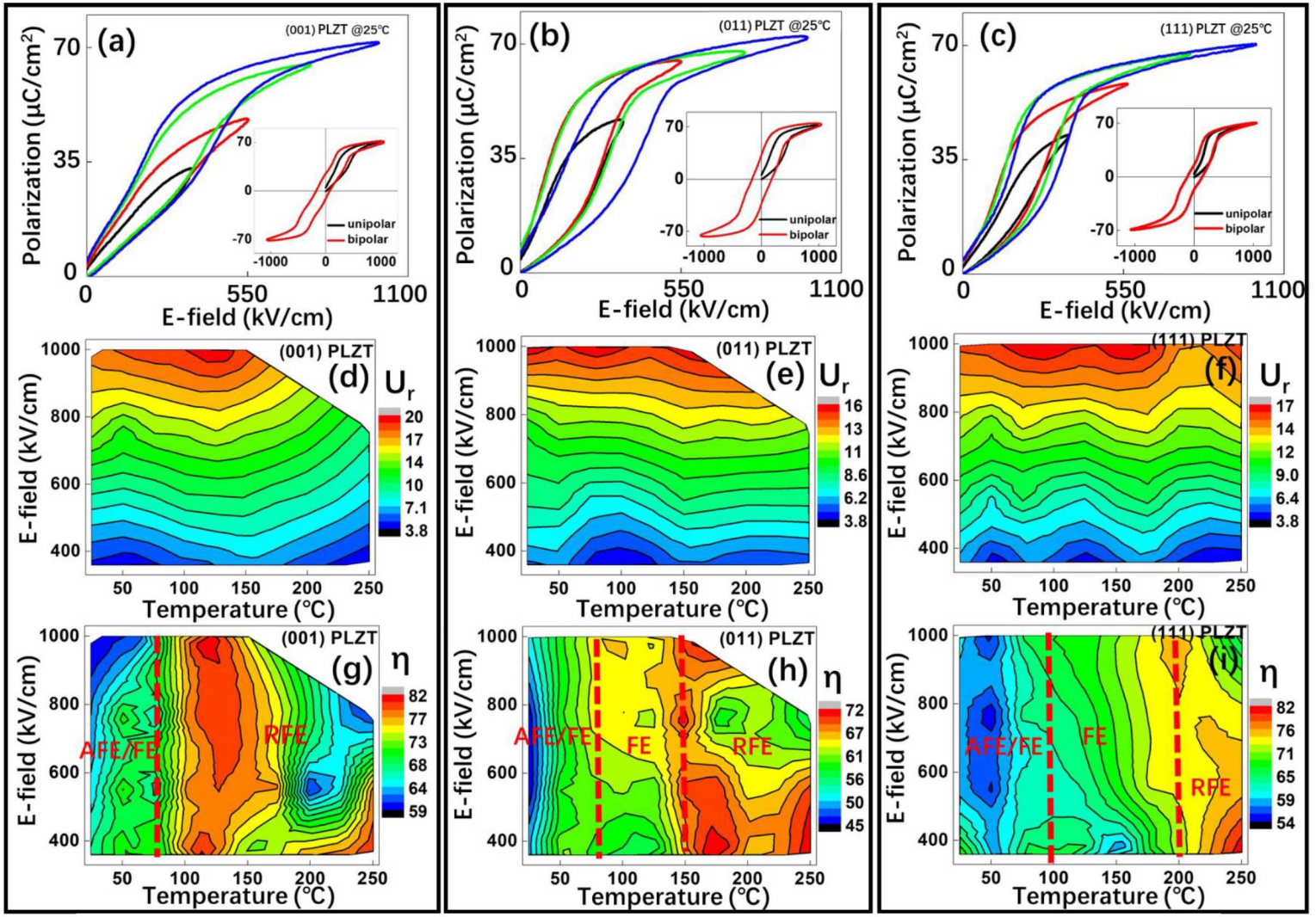

Figure 8. Unipolar P-E loops of (a) (001) PLZT, (b) (011) PLZT, and (c) (111) PLZT. The insets exhibit a comparison between unipolar and bipolar loops. (d)-(f) and (g)-(i) are the corresponding ESD (J/cm^3), and ESE (%), respectively. The red dash lines in (g)-(i) divides different phase regions based on the bipolar result characteristics.

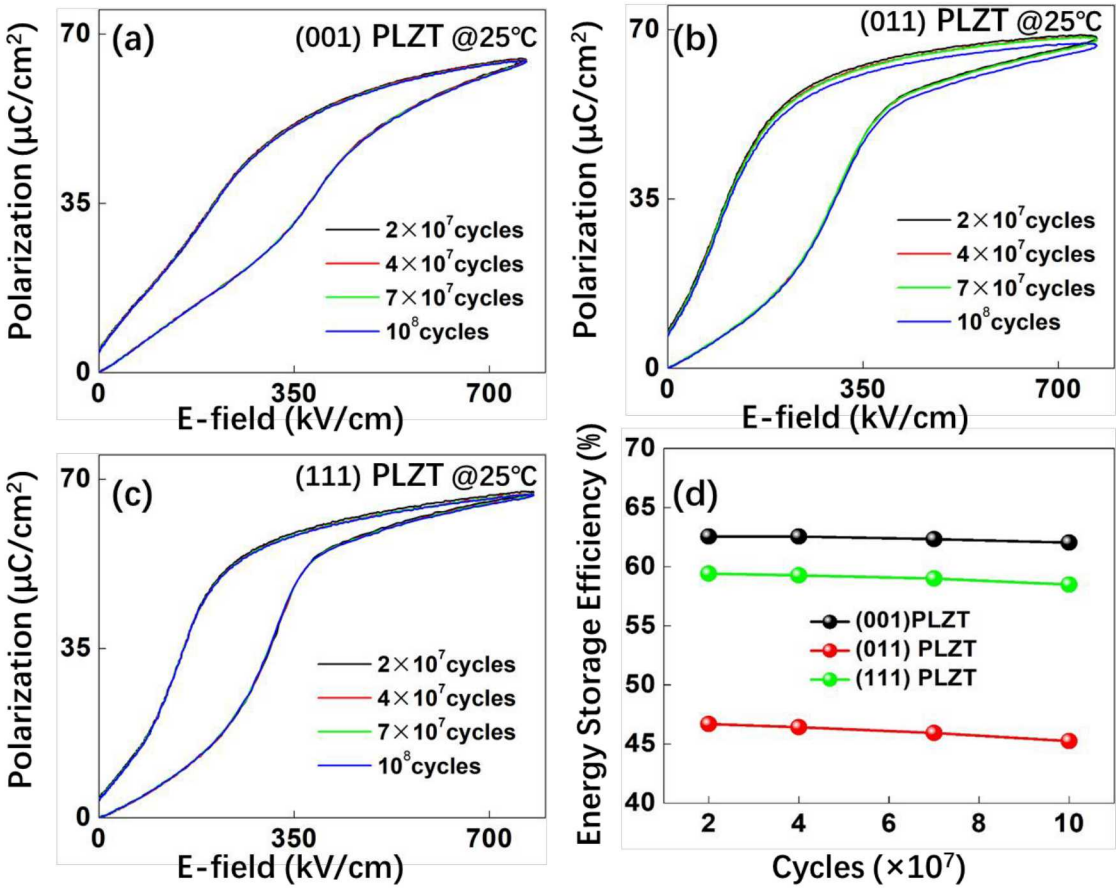

Figure 9. Unipolar P-E loops of (a) (001) PLZT, (b) (011) PLZT, and (c) (111) PLZT at room temperature with increasing numbers of charge/discharge cycles. (d) is the calculated energy storage efficiency as a function of the running cycles.